# Micro and mesoporous supports for $CO_2$ methanation catalysts: a comparison between SBA-15, MCM-41 and USY zeolite

M.C. Bacariza[a], I. Graça[b], S.S. Bebiano[c], J.M. Lopes[a], C. Henriques[a]*

[a]Centro de Química Estrutural, Instituto Superior Técnico, Universidade de Lisboa, Av. Rovisco Pais, 1049-001 Lisboa, Portugal

[b]Department of Chemical Engineering, Imperial College London, London SW7 2AZ, United Kingdom

[c]Strathclyde Institute of Pharmacy and Biomedical Sciences, Technology and Innovation Centre, University of Strathclyde, 99 George Street, Glasgow, G1 1RD, Scotland

*Corresponding author: carlos.henriques@tecnico.ulisboa.pt

## Abstract

Mesoporous SBA-15 synthesized by two different methods and MCM-41 were used as supports for Ni and Ni-Ce catalysts applied in $CO_2$ methanation reaction. The performances obtained for both materials were compared taking into account the differences in terms of textural properties, Ni species and reaction mechanism. Results were compared with the reported in the literature for a microporous USY zeolite. XRD, DRS UV-Vis, $H_2$-TPR and TEM were used for the characterization of the samples. Catalytic tests were performed under the same conditions for all catalysts. Finally, FTIR Operando studies were carried out in order to establish differences from the mechanistically point of view as well as in terms of $CO_2$ adsorption species for the different samples. Promising data was obtained with the Ni-based SBA-15 catalysts whatever the preparation method. Despite the greater Ni particles size, MCM-41 also reported interesting catalytic performances, so that presenting the highest TOF values among the catalysts studied. The good results obtained for the MCM-41 could be explained by the lower amount of non-reactive carbonyl species adsorbed on the $Ni^0$ particles surface during the reaction as well as by the enhanced interaction between metal and support reflected in the calculated band gap values. All the results are comparable to the obtained using a HNaUSY zeolite with Si/Al=2.8 as support. Cerium incorporation on Ni/mesoporous supports allowed enhancing the $CO_2$ conversion, especially at lower temperatures, as already reported for the zeolite-based samples.

**Keywords:** SBA-15, MCM-41, zeolite, nickel, $CO_2$ methanation, FTIR Operando

## 1 Introduction

$CO_2$ hydrogenation into methane could be an interesting and effective alternative for $CO_2$ emissions mitigation since it is a thermodynamically favourable reaction and methane can be used as fuel in different applications [1–3]. In terms of catalysts, the most studied metals have been noble metals (mainly Rh and Ru) and transition metals such as Ni. Nickel represents a good alternative to noble metals due to its lower cost and its high catalytic performances [4,5]. Furthermore, $SiO_2$, $Al_2O_3$, $CeO_2$, $ZrO_2$ and Ce/Zr mixed oxides have been deeply investigated as supports for methanation catalysts in the last years [4,5]. So far, few works have been published dealing with the use of micro and mesoporous materials as supports for Ni-based $CO_2$ and CO methanation catalysts [6–17], the mainly used being USY zeolite, SBA-15 and MCM-41. Ni-based USY zeolite catalysts showed interesting performances towards methanation being reported the effect of Ni content, Ce addition, the preparation method conditions and some highlights concerning the reaction mechanism [6,17–19]. In addition, SBA-15 and MCM-41 mesoporous materials were used due to their large pore sizes and interesting textural properties for the dispersion of metal species and the prevention of sintering processes. In addition, SBA-15 is known for the larger pore sizes (4.6-30 nm), higher thermal, mechanical and chemical resistance and higher surface area, when compared to MCM-41 [20]. However, no comparable data was found in the literature for the evaluation of the different micro and mesoporous materials performances in $CO_2$ methanation. As a result, the present work compares Ni catalysts containing the same amount of metal dispersed on two SBA-15 samples synthesized by different methods, a MCM-41 sample and a HNaUSY(2.8) zeolite [6]. The specific activation of nickel, evaluated from TOF determination, and the final dispersion of the metal particles over these materials are also compared. Finally, the effect of Ce incorporation to the Ni-containing mesoporous samples is also studied, in order to confirm the results previously obtained in the literature for zeolite supports [6].

## 2 Experimental

### 2.1 Catalysts preparation

All samples prepared in the present study are shown in Table 1. In terms of supports synthesis, firstly two SBA-15 supports were prepared following the methods described below. The first one, already reported in the literature [21], was named as classical method (SBA-15 CL)

and the synthesis time was of 5 days. This synthesis was performed in acid media using the tri-block copolymer Pluronic 123 (P123, Fluka) as template and tetraethyl orthosilicate (TEOS, Fluka) as silica source. In this way, P123 was dissolved in an aqueous solution of HCl (37%, Sigma Aldich) under stirring at 40ºC and, later, TEOS was added drop by drop. The final solution was kept under stirring during 2h at 40ºC. After that, a hydrothermal treatment was carried out in an oven at 100ºC for 48 h. Then, the solid was filtered and the template was removed by calcination at 550ºC during 10 h. The second method was a modification of the first one being microwaves heating applied during the hydrothermal treatment, for 2h at 170ºC (SBA-15 MW) and leading to a synthesis time of two days. Furthermore, MCM-41 was synthesised in alkaline media being cetyltrimethylammonium bromide ($C_{19}H_{42}BrN$, Aldrich) used as template and, again, tetraethyl orthosilicate (TEOS, Fluka) as silica source. Firstly, an aqueous solution of $C_{19}H_{42}BrN$ was prepared at 30ºC being kept under stirring during 15 min. Later, $NH_3$ and TEOS were added keeping the solution under stirring for 1 h. Finally, the solid was filtered and the template was removed by calcination at 550ºC during 10 h.

**Table 1.** Catalysts studied in the present work.

| | **Label** |
|---|---|
| **Zeolite-based catalysts** | 15%Ni/HNaUSY (2.8) |
| | 7%Ce15%Ni/HNaUSY (2.8) |
| **SBA-15 based catalysts** | 15%Ni/SBA-15 CL |
| | 15%Ce15%Ni/SBA-15 CL |
| | 15%Ni/SBA-15 MW |
| | 15%Ce15%Ni/SBA-15 MW |
| **MCM-41 based catalysts** | 15%Ni/MCM-41 |
| | 15%Ce15%Ni/MCM-41 |

After synthesis, SBA-15 and MCM-41 supports were impregnated by incipient wetness impregnation method [6] with 15%Ni (15%Ni/SBA-15 CL, 15%Ni/SBA-15 MW and 15%Ni/MCM-41) using nickel nitrate hexahydrate ($Ni(NO_3)_2 \cdot 6H_2O$, Sigma-Aldrich, >99%) as precursor salt. For this, a certain mass of support was weighted and an aqueous solution of nickel salt with a water volume close to that of the material pores was added to it drop by drop, being

the suspension kept under stirring. After that, samples were dried overnight at 80ºC and, finally, calcined at 500ºC under air flow. Another set of samples containing Ce additionally to Ni was prepared (15%Ce 15%Ni/SBA-15 CL, 15%Ce 15%Ni/SBA-15 MW and 15%Ce 15%Ni/MCM-41). In this case, Ni-samples were prepared as indicated before and, after calcination, Ce was impregnated following the same procedure described above and using cerium acetate sesquihydrate ($Ce(C_2OOH_3)_3 \cdot 1.5H_2O$, Alfa Aesar, 99.9%) as metal salt. The samples were also dried overnight at 80ºC and calcined at 500ºC under air flow.

In order to compare with microporous materials, two samples with similar metal contents and already reported in the literature [6] (15%Ni/HNaUSY(2.8) and 7%Ce 15%Ni/HNaUSY(2.8)) were also presented in this work.

**2.2 Catalysts characterization**

XRD patterns were obtained in a Bruker AXS Advance D8 diffractometer, using Cu Kα radiation and operating at 40 kV and 40 mA. Two different 2θ ranges were used (0.7-2.5º at a step size of 0.03º/4s and 5-80º at a step size of 0.03º/2s) in order to identify the mesoporous structure and the different oxides present in the calcined samples, respectively. XRD patterns of the spent samples were also obtained, in order to analyse the integrity of the materials structure after reaction.

In addition, DRS spectra in the UV–Vis region were obtained in a Varian Cary 5000 UV-Vis-NIR spectrophotometer equipped with a diffuse reflectance accessory in the 200–800 nm range. All reflectance spectra were converted into the Schuster – Kubelka - Munk (SKM) function (F(R)) and presented versus wavelength in order to evaluate the presence of the different Ni and Ce species in the samples.

Furthermore, $N_2$ adsorption measurements were carried out at -196ºC on a Micrometrics ASAP 2010 apparatus in order to obtain the specific surface area, mesoporous and microporous volumes and average pore diameter of the different samples. Prior to the adsorption, samples were degassed under vacuum at 90ºC during 1 h and then at 300ºC for, at least, 4 h.

To follow the study, $H_2$-TPR experiments were performed in a Micromeritics AutoChem II equipment. Catalysts were pre-treated at 250°C under argon flow and then cooled down to the

room temperature. After that, the reduction of the catalysts was carried out over a 5%$H_2$/Argon flow until 900ºC. The hydrogen consumed was monitored by a TCD detector and the reducibility of the samples was compared by representing this signal versus temperature.

Finally, TEM analysis was performed for several reduced samples (470ºC) at *Université Pierre et Marie Curie* (Paris, France) using a HRTEM 2010 JEOL LaB6 microscope (200kV) in order to evaluate the location of $Ni^0$ species as well as its average particle size.

### 2.3 Operando IR measurements

Operando IR spectra were collected using an IR cell from In-Situ Research Instruments, coupled to a Nicolet 6700 spectrometer equipped with MCT detector, by recording 50 scans at a resolution of 4 $cm^{-1}$. The different catalysts were pressed into 16mm diameter self-supported wafers of 5-20 mg and were first reduced in-situ at 450ºC for 1 h under a flow of 20mL·min−1 composed by 20% $H_2$/Ar. Samples were then cooled down by steps to 150ºC while recording different background spectra. The reduced samples were exposed to the appropriate reactive mixture ($CO_2$/Ar (5/95) or $CO_2$/$H_2$/Ar (5/20/75)) for 30 min at 150ºC and the temperature was then increased up to 450ºC while maintaining a total flow rate of 20mL$min^{-1}$. All gases were supplied by Air Liquide, with purities ≥99.9990%. Spectra were corrected to the wafers mass and difference spectra corresponding to the adsorbed species were obtained by subtracting those corresponding to the reduced fresh sample to those obtained under reactive conditions at the same temperatures.

### 2.4 Catalytic tests

Catalytic tests were performed at atmospheric pressure using a constant mass of catalyst (0.1744 g, WHSV=48 ml· $g_{cat}^{-1}$ ·$h^{-1}$). However, being zeolite and SBA-15 densities considerately different, GHSV values were affected by the support (43000 and 15000 ml·$ml_{cat}^{-1}$·$h^{-1}$). As a result, contact times for these two materials resulted in 0.08 and 0.24 s for zeolites and SBA-15/MCM-41 samples, respectively. Samples were pre-reduced at 470ºC for 1 h with an 80%$H_2$/$N_2$ flow of 250 mL $min^{-1}$. Reactivity tests were accomplished between 250-450ºC using a feed constituted by $H_2$, $CO_2$ and $N_2$ at a molar ratio of 36:9:10 (total flow=250 mL $min^{-1}$). Water present in the effluent of the reactor was removed using an ice trap before the analysis of the

products, as well as the outlet volumetric flow rate without water was measured to account for the decrease in the number of moles during the reaction. The concentrations of CO and CO2 were determined using an infrared detector and the concentration of CH4 was measured in a gas chromatograph, so that molar flow rates can be calculated and used in the evaluation of the conversion.

Turnover frequency numbers (TOF, Equation 1) were calculated for the Ni samples considering a CSTR reactor and assuming that the catalysts activity is only attributed to active Ni species with no contribution of the supports. However, if this principle can be assumed for the mesoporous based since it was found that the role of $SiO_2$ is mainly the dispersion of Ni particles [22], for the HNaUSY(2.8) zeolite, it was already reported [18] that $CO_2$ is also activated over extraframework species (EFAL) and compensating cations during methanation. Thus, the results presented for the zeolite catalysts must be carefully analysed.

$$TOF\ (s^{-1}) = x \cdot F_{Ae} \cdot (1/W) \cdot (1/n_{Ni}) \qquad \text{Equation 1}$$

**x**: $CO_2$ conversion ($mol_{CO2\ converted}/mol_{CO2\ inlet}$); $\mathbf{F_{Ae}}$: Inlet molar flow of CO2 ($mol_{CO2\ inlet}$/min); **W**: mass of catalyst in the catalytic test ($g_{catalyst}$) and $\mathbf{n_{Ni}}$: mol of Ni accessible per gram of catalyst (determined by TEM analysis considering $Ni^0$ particles as cubes with only 5 faces exposed to the reagents) ($mol_{Ni\ accessible}/g_{catalyst}$)

## 3 Results and discussion

### 3.1 Catalysts characterization

Small angle XRD diffractograms for SBA-15 and MCM-41 samples are shown in Figure 1A and Figure 2A. For the SBA-15, three well-defined peaks at 2θ ~ 0.9, 1.5 and 1.7º can be seen corresponding to the diffraction of the (100), (110) and (200) characteristic planes of the highly ordered hexagonal structure of SBA-15 [23]. The peaks attributed to the MCM-41 structure were also detected for the as-synthesized support at ~ 2.1, 4.0 and 4.6 corresponded to the (100), (110), and (200) diffraction planes of this material [24]. Introduction of Ni and Ce leads in all the cases to a decrease of the peaks intensities, which could be due the presence of the metal oxides and/or a partial damage of the ordered hexagonal pore structure specially for the MCM-41 samples in the (100) diffraction peak [13,25]. Concerning the wide angle XRD patterns (Figure 1B and Figure 2B), the presence of amorphous $SiO_2$ (broad diffraction peak around 22.3º) and NiO (37.2º, 43.3º and 62.8º) was clearly verified. Less intense peaks were observed for $CeO_2$ and

$Ce_2O_3$ (~27º, 33º, 48º and 56º). NiO was also found in the XRD patterns for the 15%Ni/HNaUSY(2.8) (13 nm), while Ce species were not detected on the 7%Ce 15%Ni/HNaUSY(2.8) sample, indicating their smaller size when compared to the mesoporous samples.

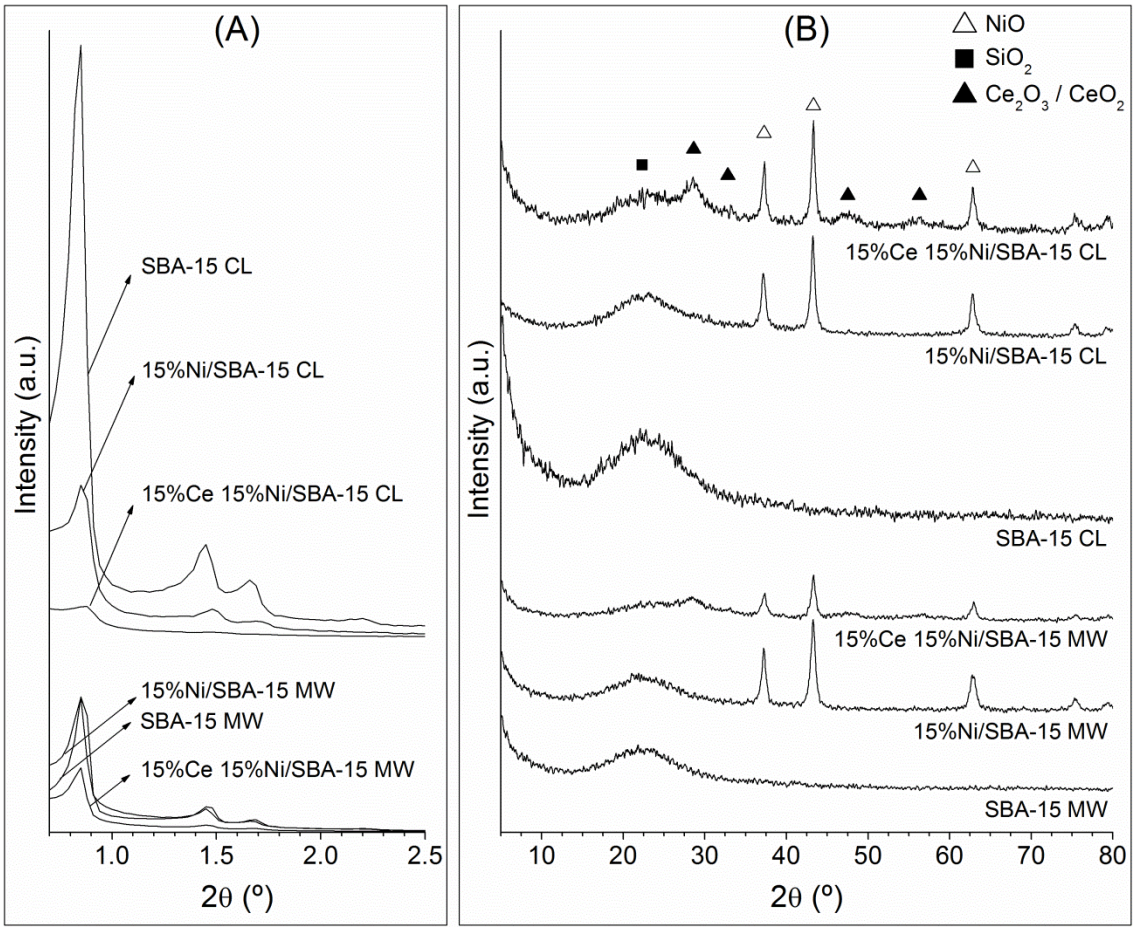


**Figure 1.** (A) Small angle and (B) wide angle XRD patterns obtained for SBA-15 samples.

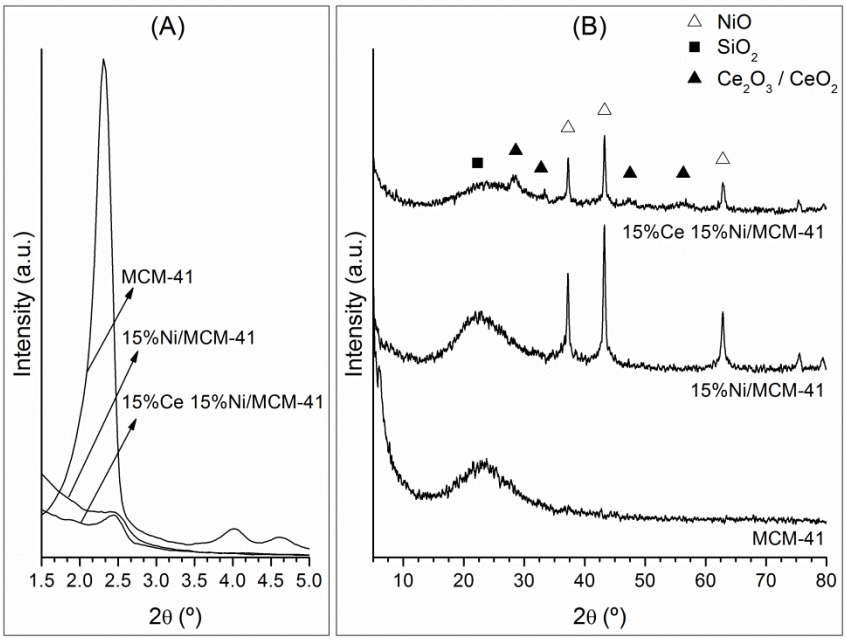


**Figure 2.** (A) Small angle and (B) wide angle XRD patterns obtained for MCM-41 samples.

Another characterization technique used for the detection of Ni and Ce species in the samples was DRS UV-Vis (Figure 3). The presence of NiO was confirmed for all Ni-impregnated mesoporous catalysts (bands at ~250, ~290 and ~320 nm as found in the literature for Ni-based SBA-15 and MCM-41 catalysts [26–28]), whereas for the 15%Ni/HNaUSY(2.8) zeolite UV bands for both NiO and $Ni^{2+}$ were observed [6]. Furthermore, bands attributed to $Ce_2O_3$ (220-265 nm) and $CeO_2$ (280-300 nm) [29–31] were found for both SBA-15 and MCM-41 samples, suggesting the presence of both type of oxides on the Ni-Ce samples. In addition, Ortega-Domínguez et al. [28] indicated that the presence of NiO clusters is characterized by the band at 320 nm, while the simultaneous presence of the three bands indicated before for NiO could indicate the coexistence of species with different sizes. Taking into account that the band at ~320 nm is less intense in the case of Ni-Ce-mesoporous materials than for the zeolite-based catalysts, one can conclude that the incorporation of Ce favours the dispersion of Ni by decreasing the size of NiO species. Indeed, for the HNaUSY(2.8) zeolite samples, NiO and $CeO_2$ bands were reported [6] but no relevant effect on the band at ~320 nm was observed.

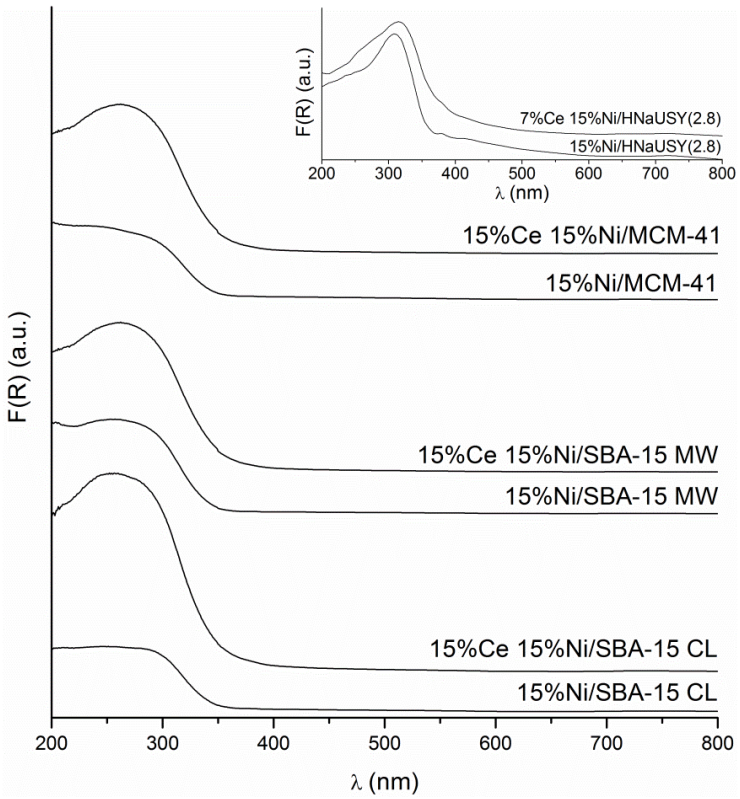


**Figure 3.** DRS UV-Vis spectra of all the samples studied in the present work as well as the obtained for the zeolite-based catalysts[6].

Table 2 shows the textural properties for all the catalysts. First of all, comparing the SBA-15 materials prepared by the two different methods, it can be seen that the SBA-15 MW support presents higher mesoporous volume and pore diameter than the SBA-15 CL, while microporous volume and $S_{BET}$ and $S_{ext}$ are lower. These results are in accordance with the literature [32], where they were explained by a destruction of the microporous system with the microwaves heating leading to a decrease of the BET surface and external surface areas. Moreover, and contrary to that found in the literature[7,33,34], a relevant decrease of the specific and external surface areas and mesoporous volumes was verified for all the supports after impregnation with Ni and Ce samples, which might be attributed to the presence of NiO and/or $CeO_2$ particles on the surface and channels of the mesoporous materials. Furthermore, no significant differences were observed in the average pore diameters after the impregnation for the SBA-15 materials, indicating that the SBA-15 porous system is preserved after metals incorporation, as also concluded by the XRD results. On the other hand, pore size decreased slightly with Ni incorporation in the MCM-41 [13], probably due to a blockage of the pore entries

by NiO particles. Nonetheless, pore size remains constant after Ce impregnation for the MCM-41 indicating that these species will be also located on the external surface of the material [35–37].

**Table 2.** Textural properties of the different samples studied on the present work.

| Sample | $S_{BET}$[a] ($m^2 . g^{-1}$) | $S_{ext}$[b] ($m^2 . g^{-1}$) | $V_{meso}$[c] ($cm^3 . g^{-1}$) | $V_{micro}$[d] ($cm^3 . g^{-1}$) | $d_{mesopores}$[e] (nm) |
|---|---|---|---|---|---|
| **HNaUSY (2.8)** | 629 | 17 | 0.032 | 0.299 | n.a. |
| **15%Ni/HNaUSY (2.8)** | n.a. | 13 | 0.031 | 0.222 | n.a. |
| **7%Ce15%Ni/HNaUSY (2.8)** | n.a. | 6 | 0.014 | 0.222 | n.a. |
| **SBA-15 CL** | 1100 | 294 | 1.262 | 0.140 | 7.8 |
| **15%Ni/SBA-15 CL** | 323 | 146 | 0.416 | 0.030 | 7.8 |
| **15%Ce15%Ni/SBA-15 CL** | 284 | 100 | 0.353 | 0.029 | 7.4 |
| **SBA-15 MW** | 703 | 182 | 1.406 | 0.070 | 8.6 |
| **15%Ni/SBA-15 MW** | 235 | 62 | 0.472 | 0.026 | 8.7 |
| **15%Ce15%Ni/SBA-15 MW** | 320 | 78 | 0.576 | 0.035 | 8.3 |
| **MCM-41** | 1017 | 23 | 0.850 | n.a. | 2.9 |
| **15%Ni/MCM-41** | 847 | 40 | 0.439 | n.a. | 1.9 |
| **15%Ce15%Ni/MCM-41** | 589 | 14 | 0.245 | n.a. | 2.0 |

[a] BET surface area [b,c,d]External surface areas and porous volumes determined by t-plot method; [e] Pore diameter determined by BJH method. NOTE: It has been reported [38] that the application of t-plot method should be used with caution when dealing with small mesopores diameters (namely, MCM-41).

Concerning $H_2$-TPR for the samples only containing Ni (Figure 4, straight lines), two main peaks attributed to NiO weakly interacting with the supports (<500ºC) and NiO strongly interacting with the supports (>500ºC) were observed [6,7,13,39–43]. The first peak is the predominant in both the SBA-15 and USY zeolite, being mostly reduced during the pre-treatment. MCM-41 Ni sample presents a relevant second reduction process at higher temperature that was attributed in the literature to the reduction of NiO species with relative lower size [44]. However, it has to be pointed out that ~46% of Ni species were estimated to be reduced for all samples during pre-treatment at 470ºC. For Ni-Ce samples, a slight shift to higher temperatures of the maximum temperatures associated to the NiO reduction peaks was generally observed whatever the support (Figure 4, dashed lines). This could be explained, according to the literature [34,45], by the order of

metals incorporation. Thus, the addition of Ce after Ni impregnation could be responsible for a reduction of the accessibility of hydrogen molecules to NiO species leading to the observed decrease in Ni species reducibility [34,45]. It has to be noted that, in the case of Ce-Ni MCM-41 catalyst, two peaks at ~ 380 and ~700ºC can also be found, which could be attributed to the reduction of NiO species with medium and strong interaction with the support and/or to the $Ce^{4+}$ reduction to $Ce^{3+}$, as reported in the literature for Ni-Ce/MCM-41 catalysts [46].

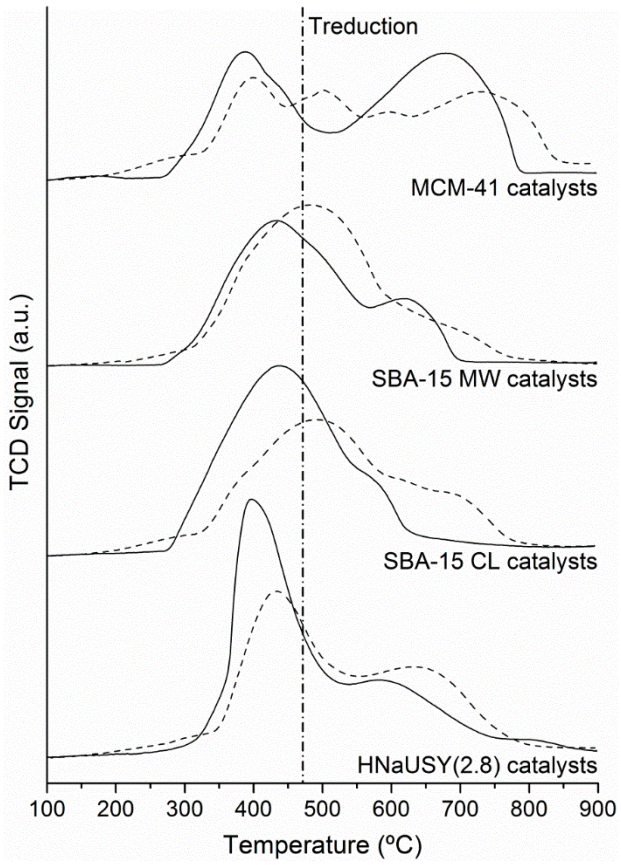


**Figure 4.** $H_2$-TPR profiles of all the samples studied in the present work. The samples profiles are presented in straight lines and dashed lines corresponding to Ni and Ni-Ce catalysts respectively.

In addition, the TEM micrographs for the reduced Ni-containing mesoporous materials are presented in Figure 5. The observation of the mesoporous channels in the TEM micrographs obtained for the reduced SBA-15 and MCM-41 catalysts allowed confirming the preservation of the structures after metals incorporation. Average $Ni^0$ particles sizes were observed to vary with the different supports as following: 15%Ni/MCM-41 (27 nm) > 15%Ni/HNaUSY(2.8) (21 nm [17])

> 15%Ni/SBA-15 CL (19 nm) > 15%Ni/SBA-15 MW (16 nm). In the case of the SBA-15 samples, some channels were observed to contain Ni particles difficult to measure, some in form of spheres and others like cylindrical aggregations inside the pores. This phenomenon was not observed for the MCM-41 sample, probably due to smaller pores sizes (~3 nm versus the ~8 nm of the SBA-15 channels). Thus, this means that $Ni^0$ particles are mainly located at the surface of the MCM-41 materials, while for the SBA-15 a fraction of particles are also located inside the pores. For the Ni-Ce samples, average $Ni^0$ particles sizes could not be calculated due to the impossibility to distinguish between Ni and Ce species in the micrographs.

**(A) 15%Ni/SBA-15 CL**

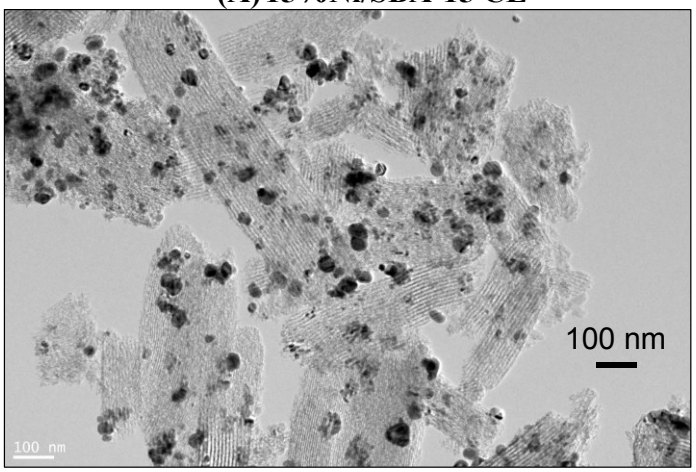


**(B) 15%Ni/SBA-15 MW**

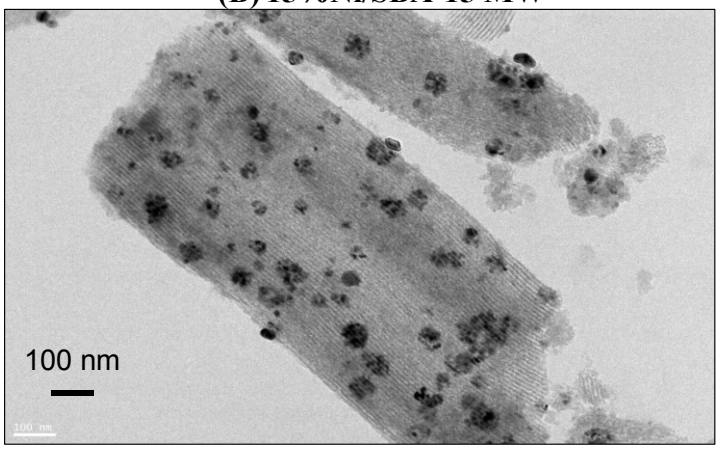


**(C) 15%Ni/MCM-41**

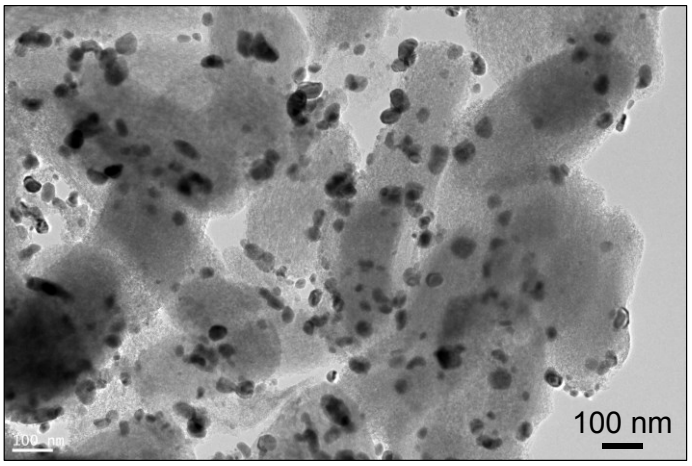


**Figure 5.** TEM micrographs for the reduced samples **(A)** 15%Ni/SBA-15 CL, **(B)** 15%Ni/SBA-15 MW and **(C)** 15%Ni/MCM-41.

Finally, the band gaps of NiO calculated from DRS UV-Vis data were compared to the $Ni^0$ sizes determined by TEM for the Ni-based catalysts (Table 3). As reported[47,48], Ni species size can influence the band gap, since the bigger the particles, the higher the amount of defects and/or vacancies present in the intergranular regions able to generate new energy levels responsible for the reduction of the band gap. Indeed, the results obtained for the samples of the present study confirm the relationship between the $Ni^0$ sizes and the calculated band gaps for NiO, indicating that the use of different supports influence the electronic properties of the Ni species.

**Table 3.** NiO band gaps, NiO and $Ni^0$ sizes in the different Ni-based samples.

| | **NiO band gap[a] (eV)** | **$Ni^0$ average size[b] (nm)** |
|---|---|---|
| 15%Ni/SBA-15 CL | 3.718 | 22 |
| 15%Ni/SBA-15 MW | 3.772 | 16 |
| 15%Ni/MCM-41 | 3.716 | 27 |
| 15%Ni/HNaUSY | 3.743 | 21 |

[a]Calculated by DRS UV-Vis data obtained for the calcined samples;
[b]Calculated by TEM micrographs of the reduced samples.

### 3.2 Evaluation of the catalytic performances

The comparison of the catalytic performances obtained for the SBA-15 samples (SBA-15 CL and SBA-15 MW), for the two types of mesoporous ordered materials (SBA-15 and MCM-

41) and for the best mesoporous catalyst and a microporous zeolite can be found in Figure 6. Results obtained for both as-synthesized SBA-15 catalysts (Figure 6A) reveal that the microwaves hydrothermal treatment leads to a catalyst with slightly higher performance, probably due to the lower $Ni^0$ size determined by TEM. When comparing the performances obtained for SBA-15 CL and MCM-41 (Figure 6B) it was observed that MCM-41 catalyst presents higher $CO_2$ conversions and similar $CH_4$ selectivity. However, the MCM-41 sample was observed to present bigger $Ni^0$ particles. Finally, when comparing the best mesoporous catalyst (15%Ni/MCM-41) with the zeolite-based sample (Figure 6C), higher $CO_2$ conversions were observed for the MCM-41 sample, even if this catalyst presented an average $Ni^0$ particle size slightly higher than the determined for the zeolite sample.

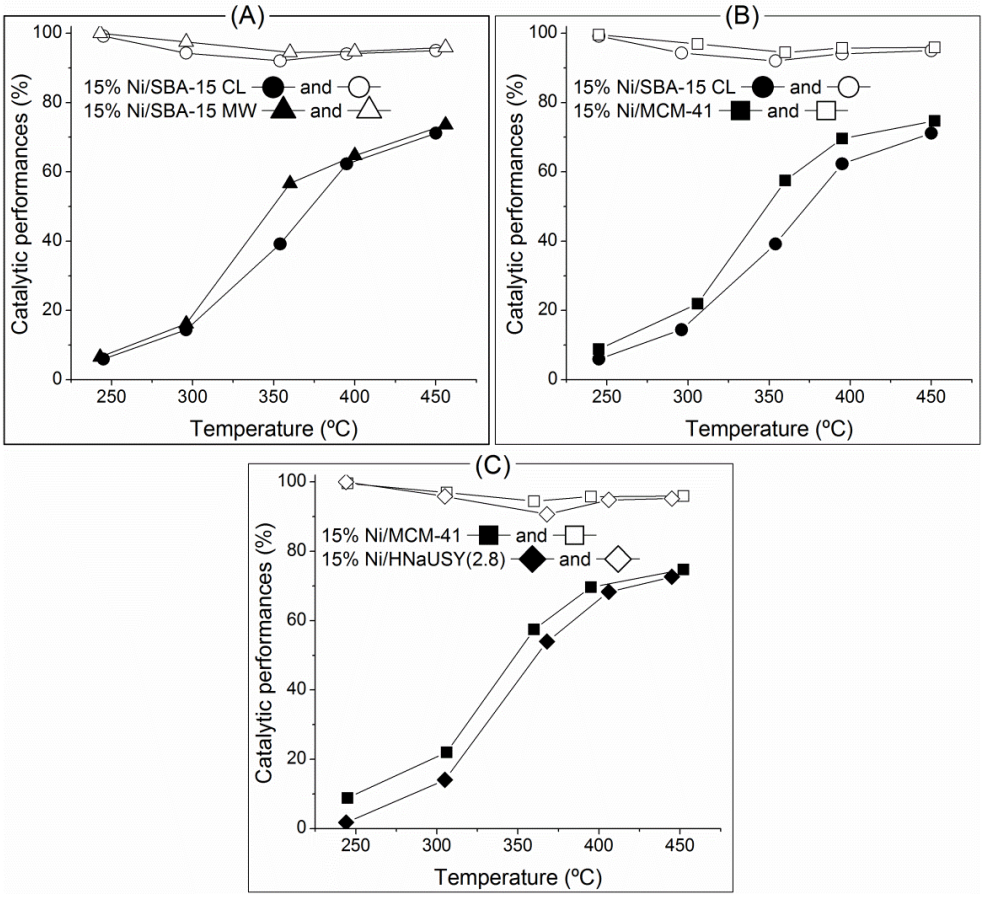


**Figure 6.** Comparison of $CO_2$ conversions (closed symbols) and $CH_4$ selectivity (opened symbols) obtained for **(A)** 15% Ni/SBA-15 CL (circles) versus 15% Ni/SBA-15 MW (triangles); **(B)** 15% Ni/SBA-15 CL (circles) versus 15% Ni/MCM-41 (squares); (C) 15% Ni/MCM-41 (squares) versus 15% Ni/HNaUSY (rhombus).

TOF numbers calculated for the different Ni samples can be found in Figure 7. According to Equation 1, TOF numbers are affected by the $CO_2$ conversion and the value of $n_{Ni}$, thus depending on the average $Ni^0$ size and the amount of $Ni^0$ in the different Ni samples. In addition, the specific activation of Ni sites depends on the interaction between the metal particle and the solid surface. Thus, when a $Ni^0$ particle is located inside a mesopore, this interaction may be probably modified. Nevertheless, it is not possible to measure such an effect, so that the calculated TOF will be an average value, taking into account all the accessible Ni atoms. Based on the $H_2$-TPR profiles, the amount of reduced Ni after pre-treatment at 470ºC is similar for all the catalysts, but the average size of the $Ni^0$ particles on the other hand depends on the support used, influencing the amount of $Ni^0$ atoms accessible to the reactants. Samples presenting NiO particles inside the mesopores (Ni/SBA-15 materials) have smaller particle size than those presenting mainly NiO species on the external surface (Ni/MCM-41 sample), and so a higher amount of Ni accessible per gram of catalyst ($n_{Ni}$). Therefore, as a consequence of the good conversions achieved and the greater Ni particle size (lower amount of exposed Ni), TOF values determined for the 15%Ni/MCM-41 catalyst are considerably higher than those calculated for the SBA-15 and zeolite samples (Figure 7). One of the reasons for the good catalytic performance obtained over the 15%Ni/MCM-41 could be the improved interaction between the Ni particles and the support reflected in the calculated band gap value. However, other factors, such as the relative quantity and the type of species adsorbed on the samples during the reaction, could also play an important role in the overall catalytic performance. These aspects will be further discussed when presenting the FTIR-operando data.

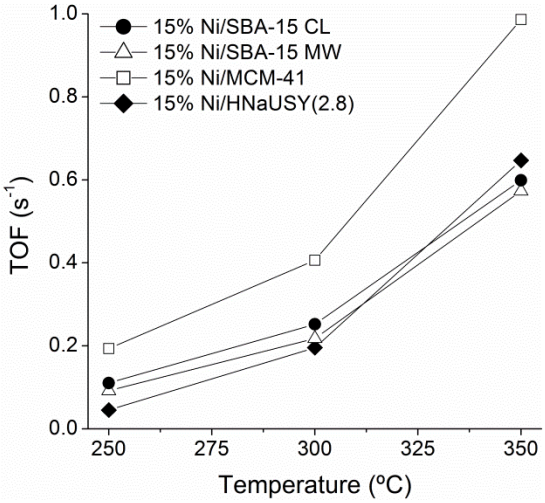


**Figure 7.** TOF numbers determined for samples 15% Ni/SBA-15 CL (circles), 15% Ni/SBA-15 MW (triangles), 15% Ni/MCM-41 (squares) and 15% Ni/HNaUSY (rhombus).

Concerning the Ni-Ce samples, much better $CO_2$ conversions and slightly higher $CH_4$ selectivity were obtained, and mainly at lower temperatures. These interesting results, already reported in the literature for similar catalytic systems, are commonly attributed to an enhancement of $CO_2$ activation on the cerium oxide species [19].

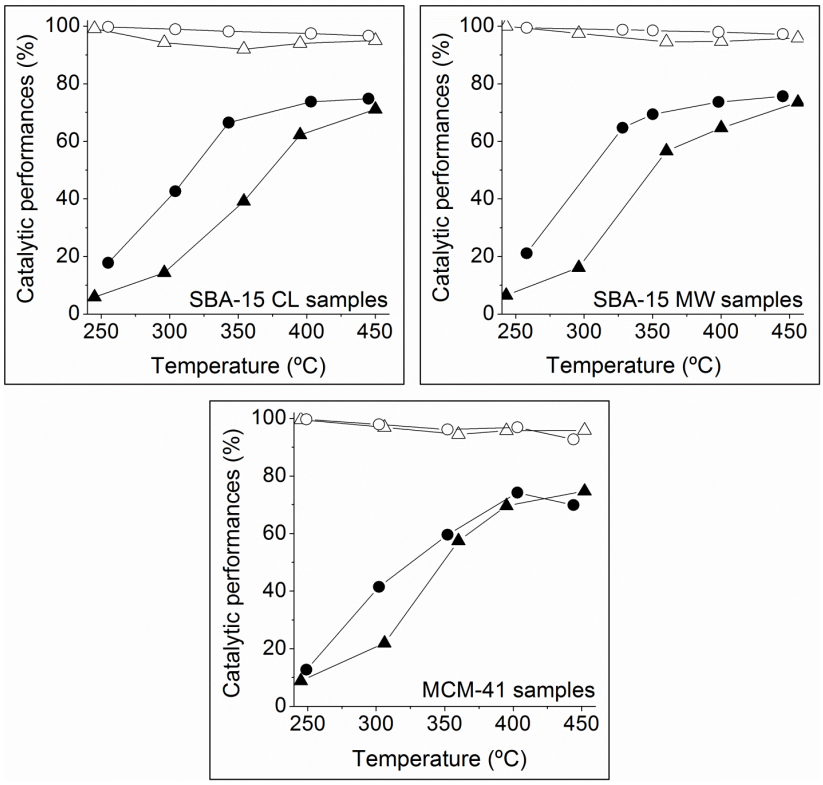


**Figure 8.** Comparison of $CO_2$ conversions (closed symbols) and $CH_4$ selectivity (opened symbols) obtained for SBA-15 CL, SBA-15 MW and MCM-41 samples containing 15% Ni (triangles) and 15% Ce-15 %Ni (circles).

After methanation, samples were characterized by XRD (Figure 9). SBA-15 catalysts preserved the three peaks attributed to the diffraction of the (100), (110) and (200) characteristic planes of the highly ordered hexagonal structure of SBA-15 at ~ 0.9, 1.5 and 1.7º [23]. On the contrary, the peaks attributed to the MCM-41 structure (~ 2.1, 4.0 and 4.6º [24]) were not clearly observed for the Ni and Ni-Ce/MCM-41 catalysts, which could be due to a migration of a greater fraction of metallic species to the pores during the catalytic test and/or a partial loss of the ordered hexagonal pore structure arrangement of the material [13,25]. Regarding the wide angle patterns, all samples presented an important decrease on the peaks intensity as already seen in the literature [26], being only observed in some cases the characteristic peaks of $Ni^0$.

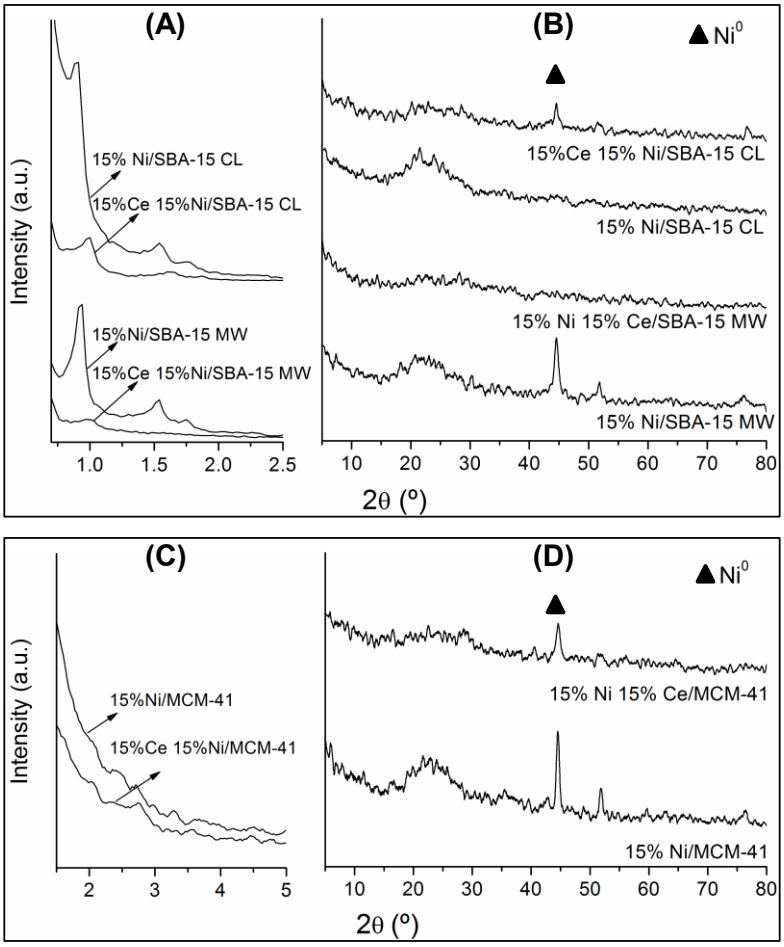


**Figure 9.** (A) Small angle and (B) wide angle XRD patterns obtained for SBA-15 samples; (C) Small angle and (D) wide angle XRD patterns obtained for MCM-41 samples.

### 3.3 FTIR-Operando studies

In order to analyse the effects of the different supports on the $CO_2$ methanation mechanism, as well as better understand the results obtained in the catalytic tests previously shown, Operando FTIR experiments were performed, including $CO_2$ adsorption/desorption and temperature programmed surface reaction (TPSR) under methanation conditions.

#### 3.3.1 Nickel incorporation effect

Methanation spectra (75%Ar/20%$H_2$/5%$CO_2$) collected at different reaction temperatures can be found in Figure 10. However, and in order to further understand these results, they must

be compared to the collected spectra for $CO_2$ adsorption (95%Ar/5%$CO_2$) at two selected temperatures with different levels of catalytic performances (Figure 11). Ni-based mesoporous samples at 150ºC+30 min under Ar/$CO_2$ conditions present mainly carbonyl species adsorbed on Ni particles (2070 to 2020 $cm^{-1}$ [22,50]), adsorbed water (1630 $cm^{-1}$ [49]), formates (~1572, ~1350 $cm^{-1}$ [17,22]), monodentate carbonates (1380 $cm^{-1}$ [18]) and methane in gas phase (1311 $cm^{-1}$ [18]). Furthermore, 15%Ni/ SBA-15 CL spectra present an intense band attributed to polycarbonates at ~1500 $cm^{-1}$ [22,51], which was not observed for the other samples. The spectra obtained after 30 min at 150ºC under Ar/$CO_2$/$H_2$ conditions present mainly the same bands as the recorded under Ar/$CO_2$. The only change is in the type and relative amount of carbonyl species adsorbed on the Ni surface, with $Ni(CO)_4$ ( 2050-2067 $cm^{-1}$ [50,52,53]) being the most favourable carbonyl specie in presence of $H_2$ for all the samples. Moroever, it is possible to see that a lower relative concentration of carbonyls is observed on the surface of the 15%Ni/MCM-41 catalyst. In addition, in the presence of $H_2$, it can be observed for all the samples a decrease of the intensity of the water band (1630 $cm^{-1}$) and of the monodentate carbonates (~1380 $cm^{-1}$), as well as an increase of the bands attributed to the formate species (~1572, ~1352 $cm^{-1}$). This indicates that these species act as reaction intermediates in the $CO_2$ methanation mechanism over all the mesoporous materials, as already reported for a Ni/$SiO_2$ catalyst [22]. Regarding the spectra recorded at 350ºC under Ar/$CO_2$ conditions, SBA-15 and MCM-41 materials presented CO in gas phase (2200-2100 $cm^{-1}$) probably due to the $CO_2$ disproportionation ($2CO_2 \rightarrow CO_{(ads)} + CO_{3(ads)}$), $CO_2$ dissociation ($CO_2 \rightarrow CO_{(ads)} + O_{(ads)}$) [54] or even to the desorption of the adsorbed CO. In addition, and as already verified at 150ºC+30min, carbonyl species are present in all the Ni samples both under Ar/$CO_2$ and Ar/$CO_2$/$H_2$, being their relative intensity compared to carbonate/formate species (1700 – 1300 $cm^{-1}$) considerably higher when compared with the spectra collected at lower temperatures.

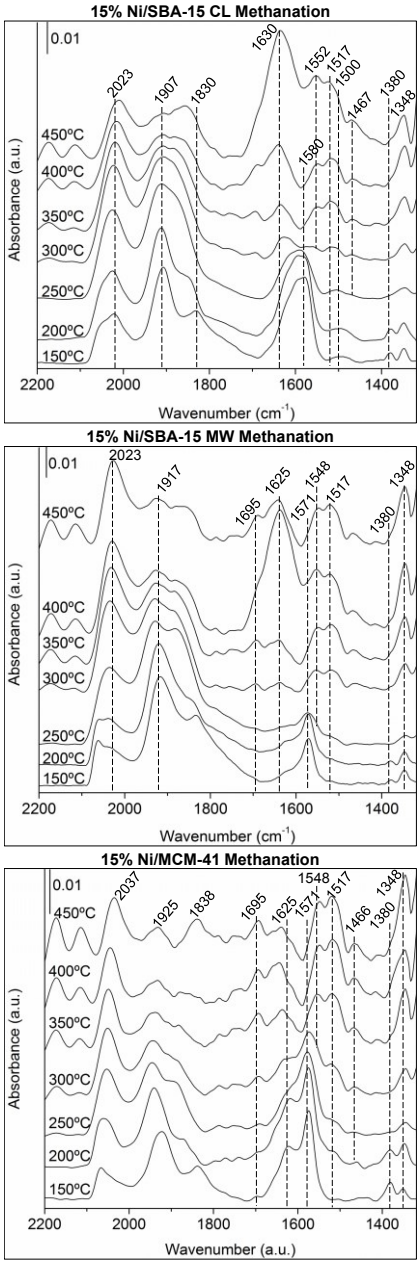


**Figure 10.** FTIR spectra collected under $CO_2$ methanation conditions over 15%Ni/SBA-158 CL, 15%Ni/SBA-15 MW and 15%Ni/MCM-41 at temperatures from 150 to 450ºC.

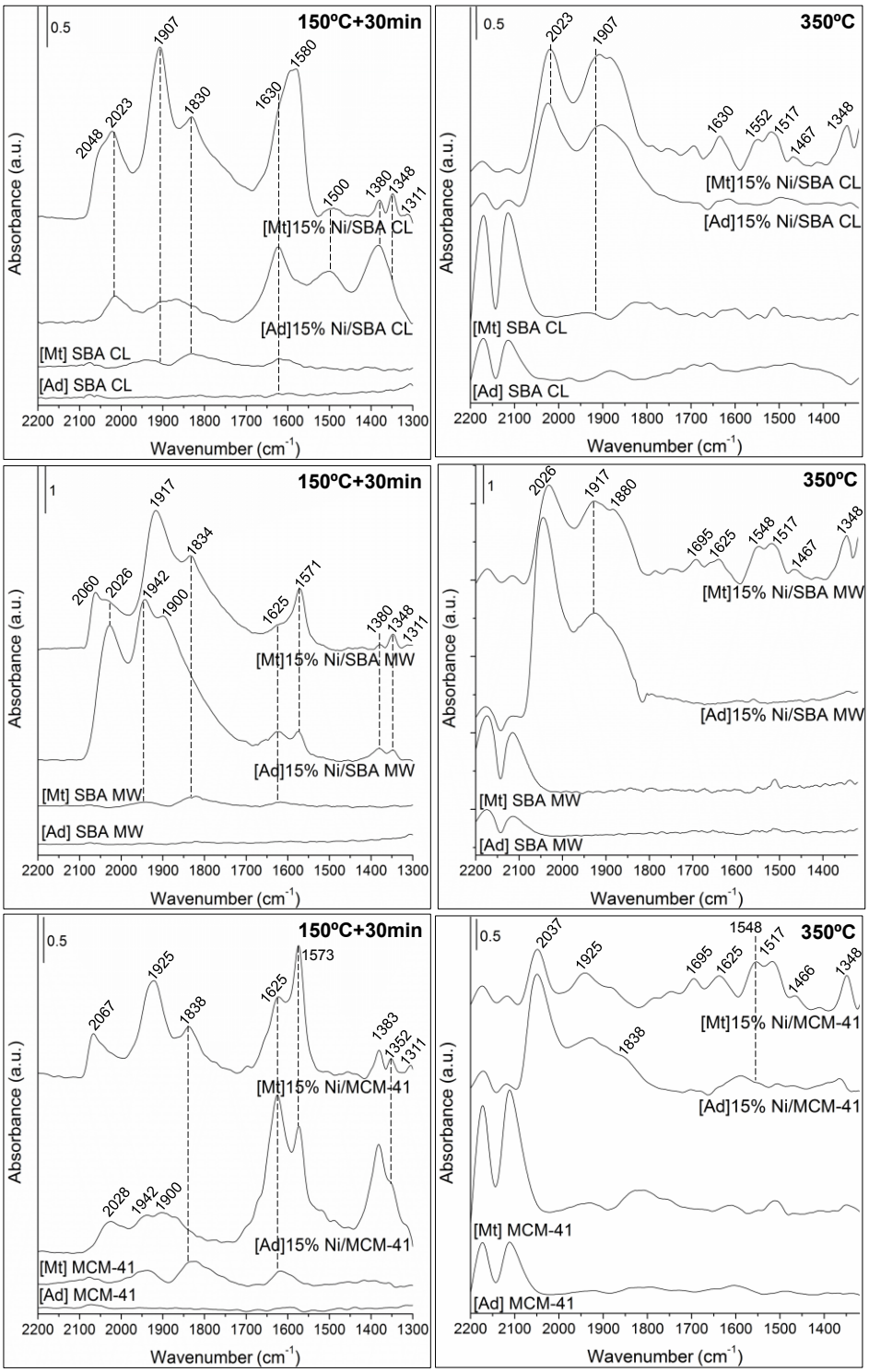


**Figure 11.** Comparison of FTIR spectra collected under $CO_2$ adsorption [Ad] and $CO_2$ methanation [Mt] conditions at 150ºC+30 min and 350ºC for samples SBA-15 CL versus 15% Ni/SBA-15 CL; SBA-15 MW versus 15% Ni/SBA-15 MW and MCM-41 versus 15% Ni/MCM-41.

As a result, and taking into account the evolution of the formates and carbonates bands in the methanation spectra presented in Figure 10, it is noticeable that the formation of carbonates due to the adsorption of $CO_2$ on the Ni sites is followed by their conversion to formates in presence of $H_2$ (methanation conditions). Thus, and following the evolution of the formate bands, it can be concluded that these species constitute an intermediate for the formation of methane, since they disappear at the temperatures where higher conversions and selectivities to $CH_4$ were found during the catalytic test. In addition, the formation of an important amount of carbonyl species (sometimes the intensity of the bands ascribed to these species was higher than the attributed to carbonate and/or formate species) on the mesoporous materials constitutes an important difference when comparing to the zeolites. When analysing the methanation spectra, one can see that the type of carbonyl species changes with the temperature being probably part of them desorbed according to the detection of CO in gas phase.

When comparing the SBA-15 CL and SBA-15 MW Ni samples, and even if the spectra presented in Figure 10 are considerably similar during the reaction, one can note that in the case of SBA-15 MW the characteristic band of water at ~1630 $cm^{-1}$ is generally less intense. As $H_2O$ is a product of the reaction, the presence of less adsorbed water in the surface of this sample could favour the $CO_2$ transformation reaction, additionally explaining the better catalytic results obtained for the SBA-15 MW than for the SBA-15 CL. Besides this, the fact that very stable polydentate carbonates were only detected for the 15%Ni/SBA-15 CL sample could also justify its lower relative methanation performance. When comparing the 15%Ni/SBA-15 CL and 15%Ni/MCM-41 samples, MCM-41 catalyst presents less intense bands attributed to carbonyl species, normally linked to Ni deactivation. Thus, these CO species adsorbed on the $Ni^0$ particles act as a poison, reducing the amount of $Ni^0$ particles available for the reaction in the 15%Ni/SBA-15 CL sample. On the other hand, in the 15%Ni/MCM-41 catalyst a higher fraction of $Ni^0$ will be available for the $H_2$ dissociation, which could justify the higher $CO_2$ conversions and TOF numbers obtained for this sample.

### 3.3.2 Cerium incorporation effect

FTIR spectra collected for Ni and NiCe samples under $CO_2$ adsorption ([Ad]) and $CO_2$ methanation ([Mt]) conditions can be observed in Figure 12. As it can be observed, the presence

of Ce influences the type of adsorbed species during the two experiments. Under $CO_2$ adsorption conditions at 150ºC+30 min, it can be seen that almost no bands related to CO carbonyls are observed, contrary to what found in the case of the Ni samples. In the spectra recorded at 350ºC, bands attributed to adsorbed water (~1620 $cm^{-1}$), monodentate carbonates (~1404 $cm^{-1}$) and formates (~1573 and ~1371 $cm^{-1}$) were also observed. As indicated before, the formation of formates under $CO_2$ adsorption conditions could be via H atoms remaining in the samples after the pre-treatments under $Ar/H_2$ flow. Under $CO_2$ methanation conditions at 150ºC+30min, it can be seen that the relative amount of formates increases whatever the mesoporous support, while the bands for carbonates decrease, indicating that the formation of the first species comes from the reaction of carbonates with H atoms. However, at higher temperature (when the $CO_2$ conversion and the $CH_4$ selectivity are considerably higher) the bands attributed to formates and carbonates species present much lower intensities, indicating that these species reacted to form $CH_4$. Thus, the presence of $CeO_2$ on the different materials studied in this work, as already reported in the literature [19,22] promotes the activation of $CO_2$ even at low temperatures, enhancing the $CH_4$ formation.

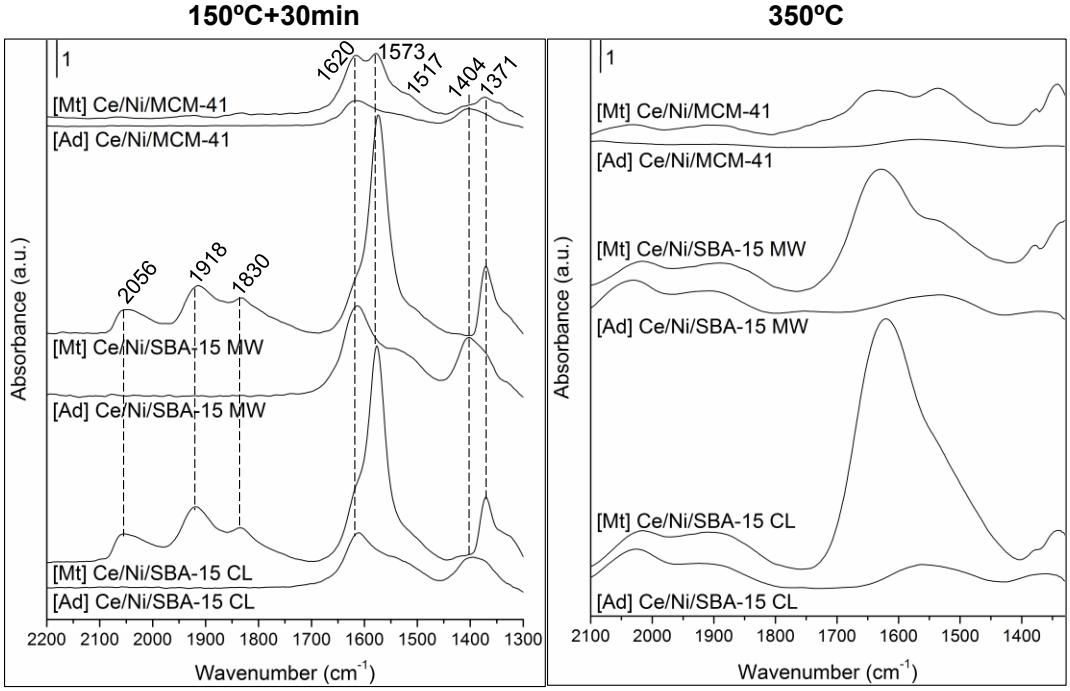


**Figure 12.** Comparison of FTIR spectra collected under $CO_2$ adsorption [Ad] and $CO_2$ methanation [Mt] conditions at 150ºC+30 min and 350ºC for samples 15% Ni/SBA-15 CL

versus 15%Ce 15% Ni/SBA-15 CL; 15% Ni/SBA-15 MW versus 15% Ce 15% Ni/SBA-15 MW and 15% Ni/MCM-41 versus 15%Ce 15% Ni/MCM-41.

## 4 Conclusions

SBA-15 synthesized by classical and microwaves-assisted methods presented similar structural and textural properties, being slightly affected after impregnation with Ni and Ni-Ce, as well as for the also synthesized MCM-41. Ni and Ce were incorporated into the supports as NiO, $Ce_2O_3$ and $CeO_2$, according to the XRD, DRS UV-Vis and $H_2$-TPR data. The reducibility of the samples at temperatures below the pre-reduction one (470ºC) was similar for SBA-15 and HNaUSY(2.8) samples, being the main reduction process attributed to the NiO species presenting weaker interaction with the support. $Ni^0$ particles sizes were affected by the support type since materials with bigger pores (e.g. SBA-15) could accommodate metal oxides allowing better metal dispersions on the catalysts surface. On the other hand, 15%Ni/MCM-41 present mainly metal species on the external surface and bigger particles due to its small pores. On the other hand, 15%Ni/MCM-41 presents mainly metal species on the external surface and bigger particles due to its small pores. In spite of the greater Ni particle size, MCM-41 Ni sample presented the highest $CO_2$ conversions, and so the best TOF numbers. These better catalytic performances could be attributed to the lower presence of carbonyl species poisoning the $Ni^0$ particles surface when compared to the SBA-15 materials, as well as to the enhanced interaction between metal and support reflected in the calculated band gap values. In addition, improved activity at low temperature was found when adding Ce due to the additional activation of $CO_2$ on $CeO_2$ species.

## Acknowledgment

M.C. Bacariza thanks to *Fundação para a Ciência e Tecnologia* (FCT) for her PhD grant (SFRK/BD/52369/2013). Authors thank also to CEOPS Project, which has received funds from the European Union's Seventh Framework Programme for research, technological development and demonstration under grant agreement number [309984].

## References


(1) Centi, G.; Perathoner, S. *Catal. Today* **2009**, *148* (3–4), 191–205.
(2) Aresta, M.; Dibenedetto, A. *Dalton Trans.* **2007**, No. 28, 2975.
(3) Aresta, M.; Dibenedetto, A.; Angelini, A. *J. CO2 Util.* **2013**, *3–4*, 65–73.
(4) Wei, W.; Jinlong, G. *Front. Chem. Sci. Eng.* **2011**, *5* (1), 2–10.
(5) Wang, W.; Wang, S.; Ma, X.; Gong, J. *Chem. Soc. Rev.* **2011**, *40* (7), 3703–3727.
(6) Graça, I.; González, L. V.; Bacariza, M. C.; Fernandes, A.; Henriques, C.; Lopes, J. M.; Ribeiro, M. F. *Appl. Catal. B Environ.* **2014**, *147*, 101–110.
(7) Tao, M.; Meng, X.; Lv, Y.; Bian, Z.; Xin, Z. *Fuel* **2016**, *165*, 289–297.
(8) Zhang, J.; Xin, Z.; Meng, X.; Lv, Y.; Tao, M. *Fuel* **2014**, *116*, 25–33.
(9) Teh, L. P.; Triwahyono, S.; Jalil, A. A.; Mukti, R. R.; Aziz, M. A. A.; Shishido, T. *Chem. Eng. J.* **2015**, *270*, 196–204.
(10) Du, G.; Lim, S.; Yang, Y.; Wang, C.; Pfefferle, L.; Haller, G. L. *J. Catal.* **2007**, *249* (2), 370–379.
(11) Lu, B.; Kawamoto, K. *Fuel* **2013**, *103*, 699–704.
(12) Tao, M.; Meng, X.; Xin, Z.; Bian, Z.; Lv, Y.; Gu, J. *Appl. Catal. Gen.* **2016**, *516*, 127–134.
(13) Zhang, J.; Xin, Z.; Meng, X.; Tao, M. *Fuel* **2013**, *109*, 693–701.
(14) Liu, Q.; Gao, J.; Gu, F.; Lu, X.; Liu, Y.; Li, H.; Zhong, Z.; Liu, B.; Xu, G.; Su, F. *J. Catal.* **2015**, *326*, 127–138.
(15) Liu, Q.; Zhong, Z.; Gu, F.; Wang, X.; Lu, X.; Li, H.; Xu, G.; Su, F. *J. Catal.* **2016**, *337*, 221–232.
(16) Hamid, M. Y. S.; Firmansyah, M. L.; Triwahyono, S.; Jalil, A. A.; Mukti, R. R.; Febriyanti, E.; Suendo, V.; Setiabudi, H. D.; Mohamed, M.; Nabgan, W. *Appl. Catal. Gen.* **2017**, *532*, 86–94.
(17) Bacariza, M. C.; Graça, I.; Westermann, A.; Ribeiro, M. F.; Lopes, J. M.; Henriques, C. *Top. Catal.* **2015**, *59* (2–4), 314–325.
(18) Westermann, A.; Azambre, B.; Bacariza, M. C.; Graça, I.; Ribeiro, M. F.; Lopes, J. M.; Henriques, C. *Appl. Catal. B Environ.* **2015**, *174*, 120–125
(19) Westermann, A.; Azambre, B.; Bacariza, M. C.; Graça, I.; Ribeiro, M. F.; Lopes, J. M.; Henriques, C. *Catal. Today* **2017**, *283*, 74-81.
(20) Nguyen, T. P. B.; Lee, J.-W.; Shim, W. G.; Moon, H. *Microporous Mesoporous Mater.* **2008**, *110* (2–3), 560–569.
(21) Zhao, D.; Huo, Q.; Feng, J.; Chmelka, B. F.; Stucky, G. D. *J. Am. Chem. Soc.* **1998**, *120* (24), 6024–6036.
(22) Aldana, P. A. U.; Ocampo, F.; Kobl, K.; Louis, B.; Thibault-Starzyk, F.; Daturi, M.; Bazin, P.; Thomas, S.; Roger, A. C. *Catal. Today* **2013**, *215*, 201–207.
(23) Yang, H.; Vovk, G.; Coombs, N.; Sokolov, I.; Ozin, G. A. *J. Mater. Chem.* **1998**, *8* (3), 743–750.
(24) Aziz, M. A. A.; Jalil, A. A.; Triwahyono, S.; Mukti, R. R.; Taufiq-Yap, Y. H.; Sazegar, M. R. *Appl. Catal. B Environ.* **2014**, *147*, 359–368.
(25) Zhao, M.; Florin, N. H.; Harris, A. T. *Appl. Catal. B Environ.* **2009**, *92* (1–2), 185–193.
(26) Lu, B.; Ju, Y.; Abe, T.; Kawamoto, K. *RSC Adv.* **2015**, *5* (70), 56444–56454.
(27) Liu, D.; Quek, X. Y.; Cheo, W. N. E.; Lau, R.; Borgna, A.; Yang, Y. *J. Catal.* **2009**, *266* (2), 380–390.
(28) Ortega-Domínguez, R. A.; Vargas-Villagrán, H.; Peñaloza-Orta, C.; Saavedra-Rubio, K.; Bokhimi, X.; Klimova, T. E. *Fuel* **2017**, *198*, 110–122.
(29) J. Roth, W.; Makowski, W.; Marszalek, B.; Michorczyk, P.; Skuza, W.; Gil, B. *J. Mater. Chem. A* **2014**, *2* (38), 15722–15725.
(30) Roth, W. J.; Gil, B.; Makowski, W.; Sławek, A.; Korzeniowska, A.; Grzybek, J.; Siwek, M.; Michorczyk, P. *Catal. Sci. Technol.* **2016**, *6* (8), 2742–2753.
(31) Bensalem, A.; C. Muller, J.; Bozon-Verduraz, F. *J. Chem. Soc. Faraday Trans.* **1992**, *88* (1), 153–154.
(32) Celer, E. B.; Jaroniec, M. *J. Am. Chem. Soc.* **2006**, *128* (44), 14408–14414.

(33) Dai, Q.; Wang, X.; Chen, G.; Zheng, Y.; Lu, G. *Microporous Mesoporous Mater.* **2007**, *100* (1–3), 268–275.
(34) Tsoncheva, T.; Issa, G.; Blasco, T.; Dimitrov, M.; Popova, M.; Hernández, S.; Kovacheva, D.; Atanasova, G.; Nieto, J. M. L. *Appl. Catal. Gen.* **2013**, *453*, 1–12.
(35) Kadgaonkar, M. D.; Laha, S. C.; Pandey, R. K.; Kumar, P.; Mirajkar, S. P.; Kumar, R. *Catal. Today* **2004**, *97* (4), 225–231.
(36) Laha, S. C.; Mukherjee, P.; Sainkar, S. R.; Kumar, R. *J. Catal.* **2002**, *207* (2), 213–223.
(37) Guevara, J. C.; Wang, J. A.; Chen, L. F.; Valenzuela, M. A.; Salas, P.; García-Ruiz, A.; Toledo, J. A.; Cortes-Jácome, M. A.; Angeles-Chavez, C.; Novaro, O. *Int. J. Hydrog. Energy* **2010**, *35* (8), 3509–3521.
(38) Galarneau, A.; Villemot, F.; Rodriguez, J.; Fajula, F.; Coasne, B. *Langmuir* **2014**, *30* (44), 13266–13274.
(39) Wang, N.; Chu, W.; Zhang, T.; Zhao, X. S. *Int. J. Hydrog. Energy* **2012**, *37* (1), 19–30.
(40) Cai, W.; Ye, L.; Zhang, L.; Ren, Y.; Yue, B.; Chen, X.; He, H. *Materials* **2014**, *7* (3), 2340–2355.
(41) Wojcieszak, R.; Monteverdi, S.; Mercy, M.; Nowak, I.; Ziolek, M.; Bettahar, M. M. *Appl. Catal. Gen.* **2004**, *268* (1–2), 241–253.
(42) Lewandowska, A.; Monteverdi, S.; Bettahar, M.; Ziolek, M. *J. Mol. Catal. Chem.* **2002**, *188* (1–2), 85–95.
(43) Wu, C.; Wang, L.; Williams, P. T.; Shi, J.; Huang, J. *Appl. Catal. B Environ.* **2011**, *108–109*, 6–13.
(44) Wu, C.; Dong, L.; Onwudili, J.; Williams, P. T.; Huang, J. *ACS Sustain. Chem. Eng.* **2013**, *1* (9), 1083–1091.
(45) Kaydouh, M.-N.; El Hassan, N.; Davidson, A.; Casale, S.; El Zakhem, H.; Massiani, P. *Comptes Rendus Chim.* **2015**, *18* (3), 293–301.
(46) Amin, R.; Liu, B. S.; Zhao, Y. C.; Huang, Z. B. *Int. J. Hydrog. Energy* **2016**, *41* (30), 12869–12879.
(47) Mohammadijoo, M.; Naderi Khorshidi, Z.; Sadrnezhaad, S. K.; Mazinani, V. *Nanoscience and Nanotechnology: An International Journal 4* (1), 6–9.
(48) Ning, X.; Lu, Y.; Fu, H.; Wan, H.; Xu, Z.; Zheng, S. *ACS Appl. Mater. Interfaces* **2017**.
(49) Lovell, E. C.; Scott, J.; Amal, R. *Molecules* **2015**, *20* (3), 4594–4609.
(50) Cormier, A. D.; Brown, J. D.; Nakamoto, K. *Inorg. Chem.* **1973**, *12* (12), 3011–3013.
(51) Köck, E.-M.; Kogler, M.; Bielz, T.; Klötzer, B.; Penner, S. *J. Phys. Chem. C Nanomater. Interfaces* **2013**, *117* (34), 17666–17673.
(52) Korányi, T. I.; Pfeifer, É.; Mihály, J.; Föttinger, K. *J. Phys. Chem. A* **2008**, *112* (23), 5126–5130.
(53) Heal, M. J.; Leisegang, E. C.; Torrington, R. G. *J. Catal.* **1976**, *42* (1), 10–19.
(54) Agnelli, M.; Swaan, H. M.; Marquez-Alvarez, C.; Martin, G. A.; Mirodatos, C. *J. Catal.* **1998**, *175* (1), 117–128.